Synthesis of High-Quality Large-Area Homogenous 1T′ $MoTe_2$ from Chemical Vapor Deposition

Lin Zhou, Ahmad Zubair, Ziqiang Wang, Xu Zhang, Fangping Ouyang, Kai Xu, Wenjing Fang, Keiji Ueno, Ju Li, Tomás Palacios, Jing Kong, and Mildred S. Dresselhaus**

2D transition-metal dichalcogenides (TMDs) have attracted increasing attention owing to their diverse properties ranging from insulator to metal and promising for wide applications.[1,2] TMDs and their 2D van der Waals heterostructures have been proposed and demonstrated in various applications, such as electronics, optoelectronics, photonics, and photovoltaics.[3,4] One TMD, $MoTe_2$, has recently been of great interest because of its special physical properties and structures. $MoTe_2$ typically exhibits two polymorphs, including a stable semiconducting 2H phase and a metastable metallic 1T′ phase.[5] The most common structure is the 2H phase, in which the Te atoms are in trigonal prismatic coordination surrounding the Mo atom. The 1T′ phase $MoTe_2$ has a monoclinic structure (distorted octahedral), which can be considered as a distortion from 1T $MoTe_2$, being driven by the Peierls distortion.[6] Monolayer and bilayer 2H $MoTe_2$ have direct bandgaps close to that of Si (≈1.1 eV), which would be ideal for integration with Si photonics.[7,8] Furthermore, 2H $MoTe_2$ exhibits strong spin–orbit coupling[9] and good thermoelectric properties,[10] all of which make it highly attractive for spintronic, valleytronic, and thermoelectric applications.

1T′ $MoTe_2$ has recently sparked great interest due to its novel features, such as large magnetoresistance,[6] pressure-driven superconductivity,[11,12] and feasibility for phase engineering.[5,13] Researchers have reported the conversion of 2H $MoTe_2$ to the 1T′ phase.[13,14] The resulting 1T′ $MoTe_2$ can then be used as a contact material for 2H $MoTe_2$-based field-effect transistors, which has the potential to solve the contact issue and greatly improve the performance of devices.[13] Furthermore, theoretical calculations predict that bulk 1T′ $MoTe_2$ is a Weyl semimetal.[11,15] 2D 1T′ $MoTe_2$ is predicted to be a class of large-gap quantum spin Hall insulators, and can be used in a topological field effect transistor, which makes use of the topological phase transition to realize fast on/off switching.[16] Therefore, the scalable production of high-quality, large-area, and uniform 2D 1T′ $MoTe_2$ is highly desirable both for rich physics research and promising electronic applications.

Previously there were several challenges for the scalable synthesis of high-quality 2D 1T′ $MoTe_2$. The inherent metastable feature of 1T′ $MoTe_2$ under ambient conditions poses a great challenge to obtain high-quality 1T′ $MoTe_2$. Moreover, the ground-state energy difference per formula unit between the 2H and 1T′ phases is quite small (≈35 meV for perfect $MoTe_2$)[5,6,13] and is sensitive to the tellurium excess/deficiency.[13] This feature suggests that synthesizing pure metastable 1T′ $MoTe_2$ without the presence of the 2H phase should be challenging. Theoretical calculations reveal that a high concentration of tellurium deficiencies can decrease the energy of 1T′ $MoTe_2$, and stabilize this metastable 1T′ phase.[13] Therefore, the 1T′ phase is always a defect-related phase. Because of the above-mentioned features, developing a synthesis method to obtain high-quality, pure 1T′ $MoTe_2$ satisfying practical requirements is challenging but crucial for its promising electronic applications and for exotic physics study.

In this work, we report the synthesis of high-quality large-area few-layer 1T′ $MoTe_2$ with high homogeneity. The as-synthesized 1T′ $MoTe_2$ films can be as thin as a few atomic layers, with high crystalline quality and excellent electrical characteristics. The 1T′ $MoTe_2$ grown from MoO_3 is of higher quality and has more homogeneity than the 1T′ $MoTe_2$ grown from Mo.

A schematic of our synthesis method is illustrated in **Figure 1**a. Typically, a Mo film (≈1 nm) is first deposited onto a SiO_2/Si substrate (growth sample) by electron beam evaporation. The growth samples are placed in a ceramic crucible containing

Dr. L. Zhou, A. Zubair, X. Zhang, Prof. F. Ouyang, Dr. W. Fang, Prof. T. Palacios, Prof. J. Kong, Prof. M. S. Dresselhaus
Department of Electrical Engineering and Computer Sciences
Massachusetts Institute of Technology
Cambridge, MA 02139, USA
E-mail: jingkong@mit.edu; millie@mgm.mit.edu
Z. Wang, Prof. J. Li
Department of Materials Science and Engineering
Massachusetts Institute of Technology
Cambridge, MA 02139, USA
Prof. F. Ouyang
School of Physics Science and Technology
Central South University
Changsha 410083, China
Dr. K. Xu
Research Institute of Petroleum Processing
SINOPEC
Beijing 100083, China
Prof. K. Ueno
Department of Chemistry
Graduate School of Science and Engineering
Saitama University
Saitama 338-8570, Japan
Prof. J. Li
Department of Nuclear Science and Engineering
Massachusetts Institute of Technology
Cambridge, MA 02139, USA
Prof. M. S. Dresselhaus
Department of Physics
Massachusetts Institute of Technology
Cambridge, MA 02139, USA

DOI: 10.1002/adma.201602687

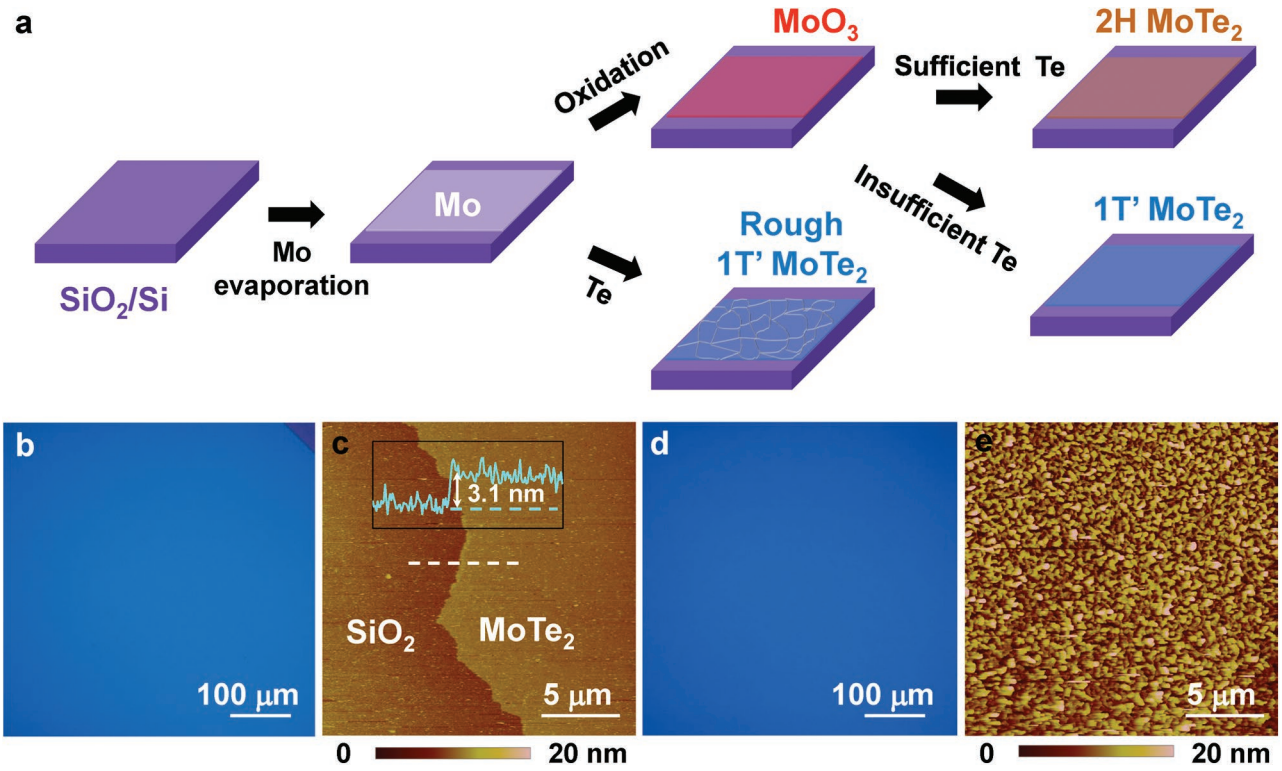

Figure 1. a) A schematic illustration of the growth process for 1T′ and 2H $MoTe_2$ using Mo and MoO_3 as precursors. b) Typical optical image of a 1T′ $MoTe_2$ film grown from MoO_3 on a 300 nm SiO_2/Si substrate. A scratch line at the upper right corner shows the bare SiO_2 substrate. c) An AFM image of the 1T′ $MoTe_2$ film grown from MoO_3. The height profile (inset) reveals that the film has a thickness of 3.1 nm. d) Typical optical image of a 1T′ $MoTe_2$ film grown from Mo. e) An AFM image of the 1T′ $MoTe_2$ film grown from Mo. Z scale, 20 nm.

Te powder and molecular sieves. For the $MoTe_2$ growth, the samples are annealed in tellurium vapor under a mixture of argon and hydrogen (Ar 3 sccm, H_2 4 sccm) gas flow at 700 °C for 1 h. Molecular sieves are essential for the $MoTe_2$ growth, because these sieves can absorb the Si_2Te_3 byproducts formed during growth and also help to release Te vapor in a controllable way for the $MoTe_2$ growth. The as-deposited Mo can directly react with Te vapor in the chemical vapor deposition (CVD) growth system, and can generate rough 1T′ $MoTe_2$ film at high temperature.[17] Another strategy is to convert the precursor from Mo to MoO_3 by full oxidation of the Mo film in air. The MoO_3 is next reacted with Te vapor and if there is sufficient Te vapor during the growth, 2H $MoTe_2$ will be obtained.[17] However, if the Te vapor during growth is insufficient, then 1T′ $MoTe_2$ will be obtained (Figure 1a). The typical growth condition for synthesizing 1T′ $MoTe_2$ is: 0.18 g Te (99.997%; Sigma–Aldrich) and molecular sieves (0.0249 g, $Na_{12}[(AlO_2)_{12}(SiO_2)_{12}]\cdot xH_2O$, 4 Å, Sigma–Aldrich) were placed in the crucible. Before heating, the whole CVD system was purged with 300 sccm Ar and 75 sccm H_2 for 1 h. Then, a mixture of 3 sccm Ar and 4 sccm H_2 was introduced into the system as a carrier gas. The system was heated from room temperature to 700 °C in 15 min, and 1T′ $MoTe_2$ was synthesized at 700 °C for 1 h under atmospheric pressure. The system was finally cooled down to room temperature by opening the furnace. 300 sccm Ar and 100 sccm H_2 flow were used to remove the reactants and to avoid oxidation of the as-grown 1T′ $MoTe_2$.

As a comparison, typical results of 1T′ $MoTe_2$ grown from two different precursors (Mo vs MoO_3 [with optimal amount of Te]) are shown in Figure 1b–e. Figure 1b,d shows optical images of 1T′ $MoTe_2$ grown from MoO_3 and Mo, respectively. The two kinds of 1T′ $MoTe_2$ films both show continuous, large-area films with no obvious difference under low magnification optical images. The surface morphologies of 1T′ $MoTe_2$ grown from Mo and MoO_3 were further characterized by atomic force microscopy (AFM). The AFM image of the 1T′ $MoTe_2$ film grown from MoO_3 (Figure 1c) reveals that this $MoTe_2$ is a uniform thin film, with a height of ≈3.1 nm in this particular sample. The $MoTe_2$ surface has a roughness of ≈1 nm, which is similar to that of the SiO_2 substrate (≈1.3 nm), suggesting a high quality material was grown. In contrast, the 1T′ $MoTe_2$ grown from Mo is much rougher (Figure 1e). The roughness of 1T′ $MoTe_2$ from Mo is ≈5 nm, much larger than the roughness of the 1T′ $MoTe_2$ obtained from MoO_3.

To investigate the uniformity and crystal quality of 1T′ $MoTe_2$ grown from different Mo precursors, Raman spectroscopy with a 532 nm excitation laser was utilized. Raman spectra were collected at 25 randomly chosen positions on the 1T′ $MoTe_2$ film grown from MoO_3 to evaluate the spatial variations of the CVD-grown film on centimeter scale. 1T′ $MoTe_2$ film has several characteristic Raman peaks in the range between 50 and 400 cm^{-1}: a prominent peak of A_g mode at ≈78 cm^{-1}, a B_g mode at ≈93 cm^{-1}, two A_g modes at ≈110 and ≈128 cm^{-1}, another prominent A_g mode at ≈162 cm^{-1}, a B_g mode at ≈189 cm^{-1},

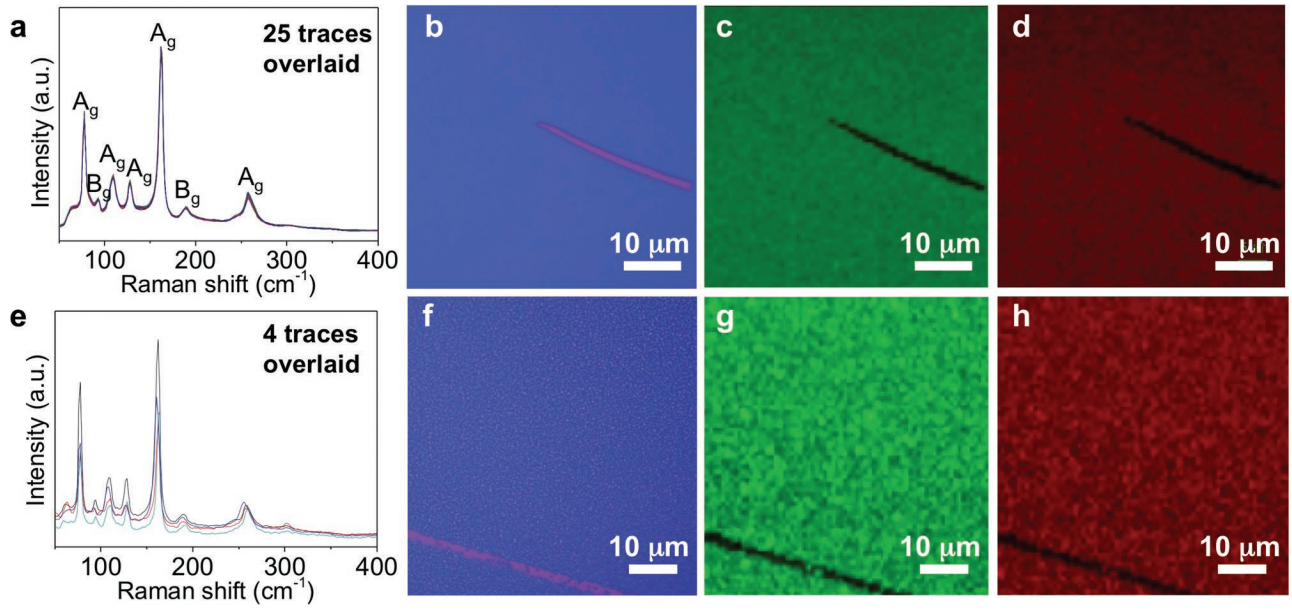

Figure 2. a) Raman spectra of the 1T′ $MoTe_2$ film grown from MoO_3 taken at 25 different locations on the sample. b) Optical microscopy image of a 1T′ $MoTe_2$ region grown from MoO_3. A scratch line (pink line) shows the bare SiO_2 substrate. b,c) Raman intensity map of the A_g peak at ≈162 cm^{-1} (c), and the A_g peak at ≈78 cm^{-1} (d) for the same region shown in (b). e) Raman spectra of the 1T′ $MoTe_2$ film grown from Mo taken at four different locations on the sample. f) Optical image of 1T′ $MoTe_2$ film grown from Mo. g,h) Corresponding Raman intensity map of peaks at ≈162 cm^{-1} (g), and the A_g peak at ≈78 cm^{-1} (h). (c,d) and (g,h) have the same intensity scales.

and an A_g mode at ≈258 cm^{-1} (**Figure 2**a). These Raman features are consistent with theoretical predictions[18] and Raman spectra of exfoliated few-layer 1T′ $MoTe_2$ (Figure S1, Supporting Information), and thus we unequivocally identify the as-grown film as being 1T′ $MoTe_2$. Moreover, the almost identical positions and intensities of the peaks in these Raman spectra taken at 25 different locations strongly suggest that the large-area 1T′ $MoTe_2$ film has high homogeneity over a centimeter scale (Figure 2a). In contrast, the Raman spectra taken at four different randomly chosen locations on 1T′ $MoTe_2$ grown from Mo shows similar Raman features; however, these four Raman spectra varied in both the peak positions and intensities of the Raman peaks (Figure 2e). This phenomenon reveals that the 1T′ $MoTe_2$ grown from Mo is inhomogeneous from location to location.

To further compare and verify the quality and uniformity of the different 1T′ $MoTe_2$ films, micro-Raman mapping with a 532 nm excitation laser was performed on 1T′ $MoTe_2$ films grown from Mo and MoO_3. The intensities of two characteristic A_g modes at ≈162 and ≈78 cm^{-1} were extracted and their spatial dependences are plotted in Figure 2c,d for the 1T′ $MoTe_2$ sample grown from MoO_3, and Figure 2g,h for the 1T′ $MoTe_2$ sample grown from Mo, respectively. Figure 2c,d reveals uniformly distributed color over the entire region, indicating the high homogeneity of the 1T′ $MoTe_2$ film grown from MoO_3 at the micrometer scale. In contrast to the highly homogenous 1T′ $MoTe_2$ from MoO_3, the spatial Raman maps of the A_g mode intensity at ≈162 cm^{-1} (Figure 2g) and ≈78 cm^{-1} (Figure 2h) of 1T′ $MoTe_2$ sample grown from Mo shows large variations, indicating the inhomogeneous nature of 1T′ $MoTe_2$ grown from Mo.

To characterize the elemental composition and bonding types in the 1T′ $MoTe_2$ film, X-ray photoelectron spectroscopy (XPS) was conducted both on the 1T′ $MoTe_2$ CVD sample grown from MoO_3 and on the 1T′ $MoTe_2$ bulk crystal synthesized by chemical vapor transport for comparison. We found that 1T′ $MoTe_2$ is easy to oxidize in the ambient atmosphere. Thus both CVD samples and bulk crystals were stored in a glove box. To avoid contamination and oxidation of the top layer of the bulk $MoTe_2$ material, we exfoliated the bulk crystal before characterization to ensure that the top surface is fresh without contamination. The handling steps take ≈30 min before the samples could be transferred into the XPS chamber, during that time the samples were exposed in air. The XPS survey spectrum of CVD grown 1T′ $MoTe_2$ reveals the presence of Mo and Te elements and has features similar with that of bulk 1T′ $MoTe_2$ (Figure S2, Supporting Information). The prominent Mo 3d peaks at 228.1 eV ($3d_{5/2}$) and 231.2 eV ($3d_{3/2}$) are assigned to Mo–Te bonds (**Figure 3**a). The Te $3d_{5/2}$ and $3d_{3/2}$ peaks, respectively, located at 572.7 and 583.1 eV, also correspond to Mo–Te bonds (Figure 3b).[17] These features match well with the XPS spectra obtained from the bulk 1T′ $MoTe_2$ crystal (Figure 3a,b). Furthermore, no Mo–O or Te–O appears in the high resolution XPS spectra of the CVD 1T′ $MoTe_2$ sample grown from MoO_3 verifies that the as-grown $MoTe_2$ is without oxide. The bulk 1T′ $MoTe_2$ shows small bumps which correspond to TeO_2 in the Te 3d XPS spectrum, indicating that a small amount of Te has been oxidized in the bulk 1T′ $MoTe_2$ sample. The results here indicate the CVD grown 1T′ $MoTe_2$ is less prone to oxidation even than bulk 1T′ $MoTe_2$, this could possibly be due to fewer defects in the sample but will need further investigation. Additionally, the atomic ratio between the Mo and Te elements

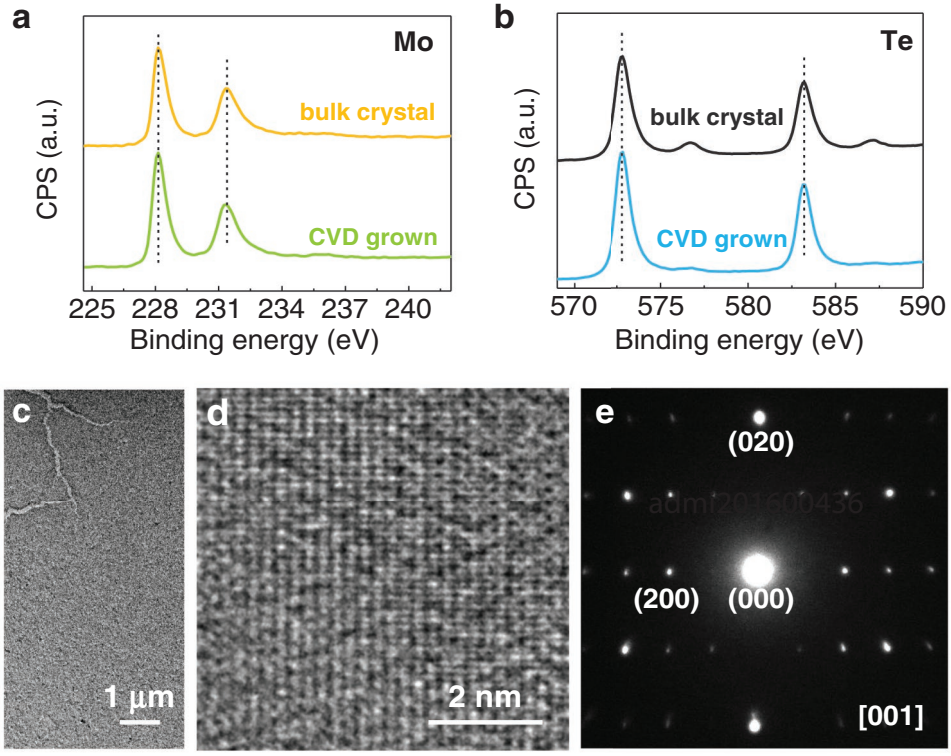

Figure 3. a,b) High-resolution XPS Mo 3d (a), and Te 3d (b) spectra of the 1T′ $MoTe_2$ film grown from MoO_3 and bulk 1T′ $MoTe_2$. c–e) Low-resolution TEM image (c), high-resolution TEM image (d), and SAED pattern (e) of the same 1T′ $MoTe_2$ film grown from MoO_3, respectively.

is 1:2.02, indicating that the 1T′ $MoTe_2$ film is stoichiometric within experimental error.

Transmission electron microscopy (TEM) was also carried out to investigate the crystallographic structure of the 1T′ $MoTe_2$ film grown from MoO_3. The CVD grown 1T′ $MoTe_2$ film was delaminated from the SiO_2/Si substrate using a diluted hydrofluoric acid solution (5%), and then transferred onto a formvar-coated slot grid. Figure 3c is a low-magnification image; a region with some cracks is intentionally chosen here so that the film can be recognized. The film is continuous and featureless, further suggesting the uniformity of the sample. High-resolution TEM of the CVD sample exhibits the expected monoclinic 1T′ structure in contrast to the hexagonal symmetry for the 2H phase, suggesting that the sample is 1T′ phase $MoTe_2$ (Figure 3d).[11] The selected area electron diffraction (SAED) pattern taken on the film reveals a rectangular pattern (Figure 3e), which is consistent with the rectangular reciprocal lattice feature of 1T′ $MoTe_2$ ($P2_1/m$ space group),[11] and further verifies that the as-obtained sample is 1T′ phase $MoTe_2$.

The electrical properties of CVD grown 1T′ $MoTe_2$ films were investigated by transport measurements. The macroscopic sheet resistance of the 1T′ $MoTe_2$ film (5 mm × 5 mm) grown from MoO_3 was measured by the van der Pauw method. The measured sheet resistance of the whole film is ≈1120 Ω sq^{-1}. The large area and uniformity of the few-layer 1T′ $MoTe_2$ film greatly facilitated the fabrication of electrical devices. We used standard electron-beam lithography (EBL) to fabricate field-effect transistor (FET) devices with various channel lengths and Hall bar devices on a Si/SiO_2 substrate, followed by e-beam evaporation of 2 nm Ti/70 nm Au as the contact metal. After EBL, the $MoTe_2$ devices were tailored into patterns using a reactive-ion etching process. The measured sheet resistance of the Hall bar devices on the same sample which excludes the contribution of contact resistance falls in a range of 1900–2028 Ω sq^{-1}. The increase of the sheet resistance after device fabrication may originate from the plasma etching process which has been found to degrade the quality of the $MoTe_2$. A typical optical image of the devices is shown in **Figure 4**a. The source-drain current versus voltage characteristic of a 1T′ $MoTe_2$ grown from MoO_3 is linear and symmetric, with a resistance of ≈155 Ω (channel length and width are 2 and 45 μm, respectively). Devices at different locations on the same 1T′ $MoTe_2$ sample grown from MoO_3 exhibit similar I–V characteristics (Figure 4b). Using the reported resistivity ≈10×10^{-6} Ω m at 300 K for bulk 1T′ $MoTe_2$,[11] and the thickness of ≈3 nm (Figure 1c) for our sample, a sheet resistance of 3.3 kΩ sq^{-1} is obtained. Our measured sheet resistance values of CVD samples before the fabrication are ≈3× less than this, suggesting the high quality and uniformity of our CVD grown 1T′ $MoTe_2$ sample.

In contrast, for the FET devices coming from the 1T′ $MoTe_2$ grown from Mo, the I_{ds}–V_{ds} curve is nonlinear and shows considerably larger resistance than the 1T′ $MoTe_2$ grown from MoO_3 (Figure 4d; Figure S3a, Supporting Information). A possible scenario for the nonlinear I_{ds}–V_{ds} could be due to the fact that the 1T′ $MoTe_2$ grown from Mo is easier to oxidize due to its relatively lower quality in comparison to the 1T′ $MoTe_2$ grown from MoO_3; the as-formed oxide layer on top of the film causes formation of a Schottky contact. By characterizing the Hall bar devices

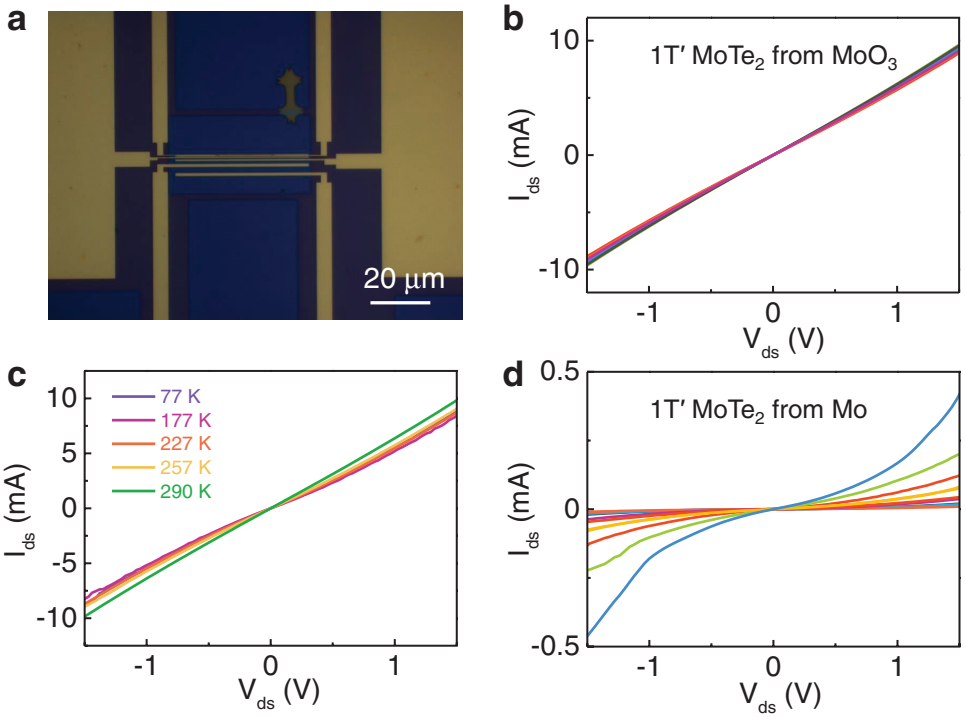

Figure 4. a) Typical optical image of devices made on 1T′ $MoTe_2$ grown from MoO_3 (blue region). b) Source–drain current (I_{ds}) vs voltage (V_{ds}) characteristics of FET devices fabricated on 1T′ $MoTe_2$ grown from MoO_3 (eight devices, the channel length and width of these FETs are 2 and 45 μm, respectively). c) Output characteristics of the device based on 1T′ $MoTe_2$ grown from MoO_3 as a function of temperature. d) Output characteristics of various FET devices of 1T′ $MoTe_2$ grown from Mo (ten devices, the channel length and width of these FETs are 2 and 45 μm).

(where the effect of the contact resistance is removed), room temperature sheet resistance values from 2000 to 6800 Ω sq^{-1} are obtained, with much wider variations compared to the 1T′ $MoTe_2$ grown from MoO_3. The large variations in sheet resistance and *I–V* characteristic curves (Figure 4d) at different locations on the same sample further suggest the inherent inhomogeneity of the 1T′ $MoTe_2$ sample grown from Mo.

Variable-temperature electrical measurements in vacuum were performed on the 1T′ $MoTe_2$ sample grown from MoO_3 and compared with values obtained from 2H $MoTe_2$ grown from MoO_3 to further investigate the electrical properties of the 1T′ phase samples. The resistance of the 1T′ $MoTe_2$ device is several orders of magnitude smaller than that of the 2H $MoTe_2$ device (Figure 4c).[17] Unlike the 2H device which shows a steady decrease of resistance with increasing temperature,[19] the resistance of the 1T′ device changes only slightly with various temperatures, suggesting the semimetal characteristics of the 1T′ phase (Figure 4c).

Our CVD 1T′ $MoTe_2$ grown from MoO_3 has considerably higher quality and better uniformity than the 1T′ $MoTe_2$ from Mo according to the characterizations by Raman, AFM, TEM, and electrical measurements. Therefore, we conclude that the Mo precursor plays a key role in determining the quality and morphology of as-grown 1T′ $MoTe_2$. Compared to metallic molybdenum, MoO_3 has some unique features: MoO_3 is hygroscopic in nature.[20] Moisture in air could be collected and help MoO_3 transport to make the MoO_3 film more uniform. More importantly, MoO_3 would diffuse and sublime during growth since MoO_3 is known to easily sublime at moderate temperature (MoO_3 begins to sublime at around 397–497 °C, melting point: 795 °C).[21] In contrast, because of the high melting point (melting point: 2620 °C), it is hard to anticipate that molybdenum atoms migrate or diffuse during growth; thus the as-grown $MoTe_2$ coming from Mo may inherit some roughness from the original Mo film after reaction with Te.

Another crucial factor to controlling the phase and quality of $MoTe_2$ grown from MoO_3 is the tellurium concentration in the $MoTe_2$ crystal. TMD materials always tend to transform to electron-rich metallic 1T and 1T′ when they have excess electrons. Therefore, chemical doping such as treating TMD material with n-butyl lithium to dope the material by electron addition is usually used to convert the 2H phase to the 1T or 1T′ phase.[22,23] In the case of $MoTe_2$, a tellurium deficiency determines the extent of electron doping, and thus determines the phase of $MoTe_2$. Theoretical calculations pointed out that the 1T′ phase should be more stable than the 2H phase under a Te monovacancy concentration above 3%.[13] In our previous work, we found that high-quality 2H $MoTe_2$ can be obtained when there is sufficient Te in the system to maintain tellurium vapor supply and avoid Te deficiency during the growth, since Te is prone to sublime at high temperature (>400 °C).[17] If the Te is insufficient and cannot maintain the Te vapor supply throughout the growth, 1T′ $MoTe_2$ will be obtained instead.

In conclusion, we have developed a method to synthesize high-quality, large-area, few-layer 1T′ $MoTe_2$ films with high homogeneity by the controlled tellurization of a MoO_3 film. The resulting 1T′ $MoTe_2$ grown from MoO_3 has high quality and uniformity, better than the 1T′ $MoTe_2$ grown from Mo.

The obtained resistivity value from our samples is even lower than those reported for bulk samples. We found that the Mo precursor plays a key role in determining the quality and morphology of the as-grown 1T′ $MoTe_2$. Furthermore, the amount of Te during growth strongly influences the phase of the $MoTe_2$ grown from MoO_3: for a sufficient Te source, 2H $MoTe_2$ would be obtained. Insufficient Te supply leads to 1T′ $MoTe_2$. The investigation of the role of the Mo precursor and the amount of tellurium for the growth of $MoTe_2$ provides insights into the controllable synthesis and phase engineering of $MoTe_2$. Our growth method enables studies of the exotic properties of 1T′ $MoTe_2$ and the scalable production of high-quality 1T′ $MoTe_2$-based applications.

Supporting Information

Supporting Information is available from the Wiley Online Library or from the author.

Acknowledgements

This study was funded by NSF grant DMR 1507806, the Center for Intergrated Quantum Materials under NSF grant DMR 1231319, and Army Research Office (ARO) (Grants W911NF-14-2-0071, 6930265, and 6930861).

Received: May 20, 2016
Revised: June 29, 2016
Published online: September 13, 2016

[1] M. Chhowalla, H. S. Shin, G. Eda, L.-J. Li, K. P. Loh, H. Zhang, *Nat. Chem.* **2013**, *5*, 263.
[2] R. Lv, J. A. Robinson, R. E. Schaak, D. Sun, Y. Sun, T. E. Mallouk, M. Terrones, *Acc. Chem. Res.* **2015**, *48*, 56.
[3] X. Duan, C. Wang, A. Pan, R. Yu, X. Duan, *Chem. Soc. Rev.* **2015**, *44*, 8859.
[4] Q. H. Wang, K. Kalantar-Zadeh, A. Kis, J. N. Coleman, M. S. Strano, *Nat. Nanotechnol.* **2012**, *7*, 699.
[5] K.-A. N. Duerloo, Y. Li, E. J. Reed, *Nat. Commun.* **2014**, *5*, 4214.
[6] D. H. Keum, S. Cho, J. H. Kim, D.-H. Choe, H.-J. Sung, M. Kan, H. Kang, J.-Y. Hwang, S. W. Kim, H. Yang, K. J. Chang, Y. H. Lee, *Nat. Phys.* **2015**, *11*, 482.
[7] I. G. Lezama, A. Arora, A. Ubaldini, C. Barreteau, E. Giannini, M. Potemski, A. F. Morpurgo, *Nano Lett.* **2015**, *15*, 2336.
[8] F. Pyatkov, V. Fütterling, S. Khasminskaya, B. S. Flavel, F. Hennrich, M. M. Kappes, R. Krupke, W. H. P. Pernice, *Nat. Photonics* **2016**, *10*, 420.
[9] N. R. Pradhan, D. Rhodes, S. Feng, Y. Xin, S. Memaran, B.-H. Moon, H. Terrones, M. Terrones, L. Balicas, *ACS Nano* **2014**, *8*, 5911.
[10] S. Balendhran, S. Walia, H. Nili, J. Z. Ou, S. Zhuiykov, R. B. Kaner, S. Sriram, M. Bhaskaran, K. Kalantar-zadeh, *Adv. Funct. Mater.* **2013**, *23*, 3952.
[11] Y. Qi, P. G. Naumov, M. N. Ali, C. R. Rajamathi, W. Schnelle, O. Barkalov, M. Hanfland, S.-C. Wu, C. Shekhar, Y. Sun, V. Susz, M. Schmidt, U. Schwarz, E. Pippel, P. Werner, R. Hillebrand, T. Forster, E. Kampert, S. Parkin, R. J. Cava, C. Felser, B. Yan, S. A. Medvedev, *Nat. Commun.* **2016**, *7*, 11038.
[12] J. D. Zhou, F. Liu, J. H. Lin, X. W. Huang, J. Xia, B. W. Zhang, Q. S. Zeng, H. Wang, C. Zhu, L. Niu, X. W. Wang, W. Fu, P. Yu, T. R. Chang, C.-H. Hsu, D. Wu, H.-T. Jeng, Y. Z. Huang, H. Lin, Z. X. Shen, C. L. Yang, L. Lu, K. Suenaga, W. Zhou, S. T. Pantelides, G. T. Liu, Z. Liu, arXiv:1606.00126.
[13] S. Cho, S. Kim, J. H. Kim, J. Zhao, J. Seok, D. H. Keum, J. Baik, D.-H. Choe, K. J. Chang, K. Suenaga, S. W. Kim, Y. H. Lee, H. Yang, *Science* **2015**, *349*, 625.
[14] S. Song, D. H. Keum, S. Cho, D. Perello, Y. Kim, Y. H. Lee, *Nano Lett.* **2016**, *16*, 188.
[15] A. A. Soluyanov, D. Gresch, Z. Wang, Q. Wu, M. Troyer, X. Dai, B. A. Bernevig, *Nature* **2015**, *527*, 495.
[16] X. Qian, J. Liu, L. Fu, J. Li, *Science* **2014**, *346*, 1344.
[17] L. Zhou, K. Xu, A. Zubair, A. D. Liao, W. Fang, F. Ouyang, Y.-H. Lee, K. Ueno, R. Saito, T. Palacios, J. Kong, M. S. Dresselhaus, *J. Am. Chem. Soc.* **2015**, *137*, 11892.
[18] M. Kan, H. G. Nam, Y. H. Lee, Q. Sun, *Phys. Chem. Chem. Phys.* **2015**, *17*, 14866.
[19] Y.-F. Lin, Y. Xu, S.-T. Wang, S.-L. Li, M. Yamamoto, A. Aparecido-Ferreira, W. W. Li, H. B. Sun, S. Nakaharai, W.-B. Jian, K. Ueno, K. Tsukagoshi, *Adv. Mater.* **2014**, *26*, 3263.
[20] G. H. Han, N. J. Kybert, C. H. Naylor, B. S. Lee, J. Ping, J. H. Park, J. Kang, S. Y. Lee, Y. H. Lee, R. Agarwal, A. T. C. Johnson, *Nat. Commun.* **2015**, *6*, 6128.
[21] Z. Song, T. Cai, Z. Chang, G. Liu, J. A. Rodriguez, J. Hrbek, *J. Am. Chem. Soc.* **2003**, *125*, 8059.
[22] R. Kappera, D. Voiry, S. E. Yalcin, B. Branch, G. Gupta, A. D. Mohite, M. Chhowalla, *Nat. Mater.* **2014**, *13*, 1128.
[23] D. Voiry, A. Goswami, R. Kappera, C. de Carvalho Castro e. Silva, D. Kaplan, T. Fujita, M. Chen, T. Asefa, M. Chhowalla, *Nat. Chem.* **2015**, *7*, 45.